Combustion and Flame 227 (2021) 384–395

Contents lists available at ScienceDirect

Combustion and Flame

journal homepage: www.elsevier.com/locate/combustflame

# PAHs controlling soot nucleation in 0.101–0.811MPa ethylene counterflow diffusion flames

Kevin Gleason, Francesco Carbone[1], Alessandro Gomez*

*Yale Center for Combustion Studies, Department of Mechanical Engineering and Materials Science, Yale University, 9 Hillhouse Avenue, New Haven, CT 06520-8286, USA*

ARTICLE INFO

*Article history:*
Received 6 October 2020
Revised 4 January 2021
Accepted 4 January 2021
Available online 27 January 2021

*Keywords:*
Soot formation
High pressure
Diffusion flames
Counterflow

ABSTRACT

On the heels of a recent study in an atmospheric pressure ethylene diffusion flame in which the transition from parent fuel molecule to Polycyclic Aromatic Hydrocarbons (PAHs) and, eventually, soot was studied by *spatially resolved* measurements of PAH concentrations and soot quantities, we extended the focus to diffusion flames with self- similar structure in the 0.101–0.811 MPa pressure range. To that end, we complemented pyrometry based measurements of soot volume fraction with light scattering measurements that, once corrected for beam steering, yielded soot particle size and number concentration profiles. A chemistry model, that had been validated for all species up to 3 ring aromatics in one of the flames investigated at each pressure and up to 4-rings for the flame at atmospheric pressure, was used to compare profiles of chemical species to those of soot quantities. Further analysis yielded the assessment of number nucleation rates of soot and their comparison to the dimerization rates of PAHs. Soot nucleation rate is consistent only with the dimerization of one- and two-ring PAHs, an observation that confirms findings in the atmospheric pressure flame. Changes in pressure and temperature have a progressively larger impact on the concentration of aromatics of increasingly larger molecular weight and, even more so, on soot volume fraction and nucleation rate. A four-fold increase in pressure from 0.101 MPa to 0.405 MPa increases the soot nucleation rate and PAH dimerization rate in flames with constant peak temperature, which is primarily a concentration effect on bimolecular collision rates; a similar but less pronounced effect is observed in the higher (0.405–0.811 MPa) pressure range. Changes in pressure and temperature tend to be progressively more consequential on aromatics of increasing molecular weight and soot.



## 1. Introduction

Soot formation has been a subject of research for decades [1–3], with recent efforts focusing on the inception stage, that is, the transition from gaseous precursors to solid particulate. A critical variable that contributes to soot formation is pressure, and high pressure is of interest because of its prevalence in practical applications, with soot formation being exacerbated under these conditions [1,3]. On the other hand, experimental work on the inception of soot tends to be focused on flames at either atmospheric pressure [4,5] or even low pressures [6,7]. As a result, there remains reasonable uncertainty concerning the extrapolation of conclusions from this body of work to high-pressure environments.

Soot inception is often modeled by considering the dimerization of PAHs such as 4-ring or larger PAHs [8–12] or resonantly stabilized radicals [4,13]. The reaction rates of these dimers are flame specific with the rates tuned to match experimentally measured soot volume fraction and particle size, but the number concentration of these large PAHs and/or radicals are low [14,15]. A measurement campaign quantifying both soot and critical PAHs in the same set of flames is needed especially at high pressures, to shed light on critical aspects of soot inception. Unfortunately, soot measurements are rarely accompanied by gaseous measurements because the presence of soot leads to clogging of the sampling probe, leaving an information gap in the path from aromatic precursors to particle inception. However, if conditions of incipient soot formation are established, measurements of both gaseous precursors and soot particles are available [15,16], building confidence in models predictions of some of the critical soot precursors such as $C_2H_2$, $C_6H_6$, small PAHs (i.e., with less than 3-rings), and, in some cases [15], even relatively large (i.e., 6-ringed) PAHs. This type of data provides a direct comparison of gaseous precursors and soot

* Corresponding author.
*E-mail address:* alessandro.gomez@yale.edu (A. Gomez).
[1] Current Address: Department of Mechanical Engineering, University of Connecticut, 191 Auditorium Road, Unit 3139, Storrs, CT 06269–3139, USA.

https://doi.org/10.1016/j.combustflame.2021.01.015
0010-2180/

particles to assess which PAHs control ultimately the soot nucleation rate.

Limiting measurements to only incipiently sooting flames provides a very narrow range of conditions to explore how key parameters such as pressure and temperature influence soot formation. Alternatively, so long as the perturbed flames do not depart significantly from the validated flames, one can rely on a partially-validated chemistry model to predict the gaseous precursors in perturbed flames with an increased soot load that would be otherwise incompatible with microprobe sampling of the gas precursors [16,17]. This is the approach followed in the present study by relying on a set of counterflow flames with a self-similar structure.

These flames are chosen as a convenient theater to track the evolution of fuel to soot thanks to their one-dimensionality and suitability to high pressures through the avoidance of buoyant instabilities [18]. Viable soot measurement techniques in such flames include pyrometry, to quantify the volume fraction and dispersion exponent [16], light extinction and laser induced incandescence to quantify soot volume fraction and particle size [19–21]. Pyrometry is advantageous because it is minimally affected by the steep temperature/density gradients. Laser diagnostics, on the other hand, are plagued by beam steering, although ray-tracing algorithms can correct for it if measurements are performed in two dimensions [22]. Pointwise line-of-sight measurements may be less influenced by beam steering, but they lack the necessary spatial resolution at high pressures and are difficult to implement in the soot inception zone because of flame curvature and two-dimensional effects [19]. Measurements were performed in high-pressure co-flow flames [3,23–26], but they focused on mature soot rather than the inception stage, in addition to presenting the drawback of two-dimensionality.

This work is an extension of [16] introducing two important novelties: first, it complements previous measurements of volume fraction with particle size via laser light scattering. To that end, an approach is developed to correct for the inevitable beam steering in high-pressure flames, improving the accuracy of measuring the gas phase Rayleigh scattering contribution and ultimately allowing for the quantification of the smallest (2–3 nm) soot particles. Second, it capitalizes on an extensive database regarding the chemical structure of self-similar flames in the investigated pressure range including species up to 3-ring aromatics [27] and recent work at atmospheric pressure that determined *spatially resolved* profiles of the concentration of PAHs composed of as many as 6-rings [15]. The comparison of the experimental results with model predictions offered the (partial) validation of the kinetic model and enabled us to use its predictions in the high-pressure flames of the present study. With measurements of soot at the onset of nucleation along with measurements and/or reliable predictions of gaseous precursors, we compared soot nucleation rates to those of PAHs and assessed which PAHs control soot nucleation in counterflow diffusion flames of ethylene in the 0.101–0.811 MPa pressure range. We also established the pressure and temperature dependence on soot inception and growth.

## 2. Methods

### 2.1. Flame selection and modeling

The counterflow burner is described in detail in [28]. The burner consists of two identical nozzles converging to an outlet internal diameter of 6.35 mm and separated by a distance $L = 8$ mm. Both nozzles are surrounded by conical enclosures to flow shroud nitrogen and shield the flame from external disturbances. Calibrated flows of nitrogen/ethylene and of nitrogen/oxygen are fed to the bottom nozzle and top nozzle, respectively. The boundary conditions of all the investigated flames are listed in Table 1, including: mole fractions, mass average velocity, and the computed maximum flame temperature. Rows in bold pertain to flames that have been characterized with GC/MS and temperature measurements [15,27] whereas those in italics above the bold ones refer to flame for which the scattering contributions from soot cannot be distinguished experimentally from that of the gas molecules. All flames are flat in proximity to the burner axis, as verified by digital imaging, and will be treated as one-dimensional in computational modeling and data analysis.

This work is aimed at complementing previous measurements of soot volume fraction [16,17] by quantifying particle size and number concentration via laser light scattering. The additional information will enable us to make a direct comparison between incipient soot formation and the formation of aromatics to assess which are the critical species in the evolution to soot. Starting from incipiently sooting diffusion flames at 0.101 MPa, 0.405 MPa, and 0.811 MPa, we study the effect of temperature and pressure on soot formation and growth by perturbing such flames at constant stoichiometric mixture fraction, $Z_{st}$, and global strain rate, $a$, to control the maximum flame temperature, $T_{max}$, in increments of approximately 50 K, bracketing the flames that were characterized by GC/MS and temperature measurements [27]. The constancy of $Z_{st}$ and $a$ ensures that the relative position of flame and Gas Stagnation Plane (GSP) is unchanged at a fixed pressure and that flames are reasonably self-similar with respect to temperature and gaseous species [16,17] at different pressures. Such a characteristic allows one to isolate $T_{max}$ as a controlling parameter. Mass averaged velocities of fuel, $V_f$, and oxidizer, $V_{ox}$, streams are selected to ensure momentum flux balance ($\rho_f V_f^2 = \rho_{ox} V_{ox}^2$) and are approximately constant for the investigated flames.

Flames are modeled with ANSYS CHEMKIN-Pro [29] and the CRECK 2015 chemistry mechanism [30]. The velocity boundary conditions were corrected for departures from plug flow as described in [27]. The axial velocity and velocity gradient are nearly independent of $T_{max}$ as verified in the atmospheric pressure flames [17], so the velocity boundary conditions are assumed fixed at each pressure as listed in Table 2 [27]. Heat losses due to the thermal radiation emitted by $CH_4$, $H_2O$, CO, and $CO_2$ were evaluated by emission band integration in the optically thin limit [31]. Heat losses associated with soot emission were not included in the model but were estimated using the approach detailed in [32] and found to be significantly smaller than those due to gas radiation because of the light soot loading of the investigated flames.

### 2.2. Experimental methods

Planar light scattering measurements are performed with the (532 nm) second harmonic of a 10 ns pulsed Nd:YAG laser (New Wave Gemini PIV). A cylindrical lens shapes the laser beam into a 4 mm by 1 mm sheet at the center of the burner with the laser fluence kept below 100mJ/cm$^2$ to ensure that soot particles are not ablated by the high energy pulses [33]. The scattered light is imaged onto an intensified camera (12-bit PCO DiCAM-Pro) positioned at a 90° scattering angle, through an optical train including an 80 mm macro lens, a polarizer, and a 532nm±10 nm interference filter. The pixel resolution is 22.7 µm/pixel. Data analysis is performed on an average of 500 images captured in a 20 ns gating window and background subtraction is applied by imaging the flame with the laser off. The gas-phase total light scattering coefficient of the investigated flames is calculated using the computed number concentration of the following gases: $H_2$, $H_2O$, $N_2$, $O_2$, $CH_4$, CO, $CO_2$, $C_2H_2$, $C_2H_4$, $C_2H_6$, $C_3H_8$, $C_3H_4$, $C_4H_6$, and $C_6H_6$ whose scattering cross-section are reported in the literature [34–37]. These 14 species account for more than 99% of the flames molar composition at any axial position, the remaining <1% is due to a multitude of small radicals and multiring PAHs whose

**Table 1**
Computed peak flame temperature and boundary conditions (mole fractions and mass averaged velocity). All flames have constant stoichiometric mixture fraction ($Z_{st}$=0.183) and global strain rate ($a$=($V_{avg\text{-}f}$+$V_{avg\text{-}ox}$)/$L$ = 50s$^{-1}$). Bold rows pertain to the only flames characterized with GC/MS and temperature measurements [27] and italicized rows above those in bold pertain to flames that do not have a measurable light scattering signal from soot particles.

| | | Fuel Stream ($T$ = 298 K) | | | Oxidizer Stream ($T$ = 323 K) | | |
|---|---|---|---|---|---|---|---|
| | T (K) | $C_2H_4$ | $N_2$ | $V_{avg}$ (cm/s) | $O_2$ | $N_2$ | $V_{avg}$ (cm/s) |
| 0.101MPa | *1922* | *0.305* | *0.695* | *20.2* | *0.211* | *0.789* | *19.8* |
| | *1960* | *0.315* | *0.685* | *20.2* | *0.218* | *0.782* | *19.8* |
| | **2013** | **0.330** | **0.670** | **20.2** | **0.229** | **0.771** | **19.8** |
| | 2063 | 0.345 | 0.655 | 20.2 | 0.240 | 0.760 | 19.8 |
| | 2113 | 0.360 | 0.640 | 20.2 | 0.250 | 0.750 | 19.8 |
| | 2160 | 0.375 | 0.625 | 20.2 | 0.261 | 0.739 | 19.8 |
| | 2207 | 0.390 | 0.610 | 20.2 | 0.272 | 0.728 | 19.8 |
| 0.405MPa | *1665* | *0.225* | *0.775* | *20.1* | *0.155* | *0.845* | *19.9* |
| | *1721* | *0.235* | *0.765* | *20.1* | *0.162* | *0.838* | *19.9* |
| | *1775* | *0.245* | *0.755* | *20.1* | *0.168* | *0.832* | *19.9* |
| | ***1826*** | ***0.255*** | ***0.745*** | ***20.1*** | ***0.176*** | ***0.824*** | ***19.9*** |
| | 1875 | 0.265 | 0.735 | 20.1 | 0.183 | 0.817 | 19.9 |
| | 1923 | 0.275 | 0.725 | 20.1 | 0.190 | 0.810 | 19.9 |
| | 1970 | 0.285 | 0.715 | 20.1 | 0.197 | 0.803 | 19.9 |
| | 2016 | 0.295 | 0.705 | 20.1 | 0.204 | 0.796 | 19.9 |
| 0.811MPa | *1556* | *0.205* | *0.795* | *20.1* | *0.140* | *0.860* | *19.9* |
| | *1635* | *0.215* | *0.785* | *20.1* | *0.147* | *0.853* | *19.9* |
| | ***1696*** | ***0.225*** | ***0.775*** | ***20.1*** | ***0.155*** | ***0.845*** | ***19.9*** |
| | *1754* | *0.235* | *0.765* | *20.1* | *0.161* | *0.839* | *19.9* |
| | 1809 | 0.245 | 0.755 | 20.1 | 0.168 | 0.832 | 19.9 |
| | 1862 | 0.255 | 0.745 | 20.1 | 0.176 | 0.824 | 19.9 |
| | 1914 | 0.265 | 0.735 | 20.1 | 0.183 | 0.817 | 19.9 |

**Table 2**
Velocity and velocity gradient boundary conditions computed with 2D modeling [15,27] to account for deviations from plug flow.

| | 0.101MPa | 0.405MPa | 0.811MPa |
|---|---|---|---|
| Fuel stream | | | |
| $V_{avg}$ (cm/s) | 20.2 | 20.1 | 20.1 |
| $V_{ax}$ (cm/s) | 27.8 | 23.4 | 21.6 |
| $dV/dz$ (s$^{-1}$) | 26.4 | 17.4 | 16.2 |
| Oxidizer stream | | | |
| $V_{avg}$ (cm/s) | 19.8 | 19.9 | 19.9 |
| $V_{ax}$ (cm/s) | 34.1 | 28.3 | 25.9 |
| $dV/dz$ (s$^{-1}$) | 16.2 | 9.15 | 8.54 |

contribution was estimated assuming an average value for their scattering cross-section. All species accounted for in gas phase scattering, except for $H_2O$, were measured and quantified with the GC/MS in one flame at each pressure [15,27].

Rayleigh scattering calibrations are performed with propane, ethylene, and nitrogen to verify that the appropriate ratios of the scattering coefficient are obtained. The calibration gas is flowed through both top and bottom nozzles and imaged onto the intensified camera using the same experimental parameters (laser power, camera gating time, chamber pressure, etc.) that are used during the in-flame measurements. The calibration of any one gas ('*cali*') is used to convert the measured Rayleigh signal $S$ to the scattering coefficient $Q_{vv}$,

$$Q_{vv} = S_{meas}\frac{NC_{vv}^{cali}}{S_{cali}} \tag{1}$$

where $N$ is the local gas number density and $C_{vv}$ is the scattering section of the calibration gas with the subscript '$vv$' referring to both incident and scattered vertically polarized light. The soot number concentration $N_s$ is evaluated under the hypothesis of size monodispersity as

$$N_s = \frac{9\pi^2 F(m) f_v^2}{Q_{vv}^{soot}\lambda^4}, \tag{2}$$

where $Q_{vv}^{soot}$ is the measured excess scattering coefficient attributed to soot, net of the Rayleigh scattering contribution from the gas phase, $f_v$ is the measured soot volume fraction via pyrometry [16], and $F(m) = 0.69\pm0.13$ is the dimensionless refractive index function at the laser wavelength $\lambda = 532$ nm based on the relationship between $F(m)$ and the dimensionless extinction coefficient [38]. The soot particle diameter is evaluated by

$$d = \left(\frac{6f_v}{\pi N_s}\right)^{1/3} \tag{3}$$

under the assumption of spherically shaped particles that are monodisperse in size. The error bars on the measured soot number concentration and particle diameter are estimated through error propagation by applying general uncertainty analysis to Eqs. (2) and (3).

The soot volume fraction is measured by pyrometry imaging the flame onto a Nikon D70 camera with a 210 mm focal length lens stopped at f/8. Measurements are performed by averaging 20 images. Images are split into red, green, and blue color channels and deconvolved into a two-dimensional field using an Abel transform [39]. The soot volume fraction is evaluated through

$$f_v = -\frac{\lambda_e}{\tilde{K}_{ext}L_p}\ln\left\{1-\epsilon_c(\lambda_e)\frac{\tau_c S_s}{\tau_s S_c}\exp\left[-\frac{hc}{k_B\lambda_e}\left(\frac{1}{T_c}-\frac{1}{T_s}\right)\right]\right\}, \tag{4}$$

where $\lambda_e$, $\tilde{K}_{ext}$, $L_P$, and $\tau$ are the effective wavelength of the color channel, dimensionless extinction coefficient, pixel length, and exposure time, respectively. The subscripts $c$ and $s$ refer to the calibration and measurements on soot particles, respectively. An S-type thermocouple is used as a light calibration source [40]. We assume a constant $\tilde{K}_{ext} = 5.34\pm2.68$ [17]. The temperature of soot, assuming thermal equilibrium between soot particles and gas phase, is based on one-dimensional modeling that has been validated by thermocouple measurements [15,17,27]. The uncertainty in the computed temperature is ±16 K throughout the entire soot forming region based on the uncertainty in stream composition and velocity of both streams.

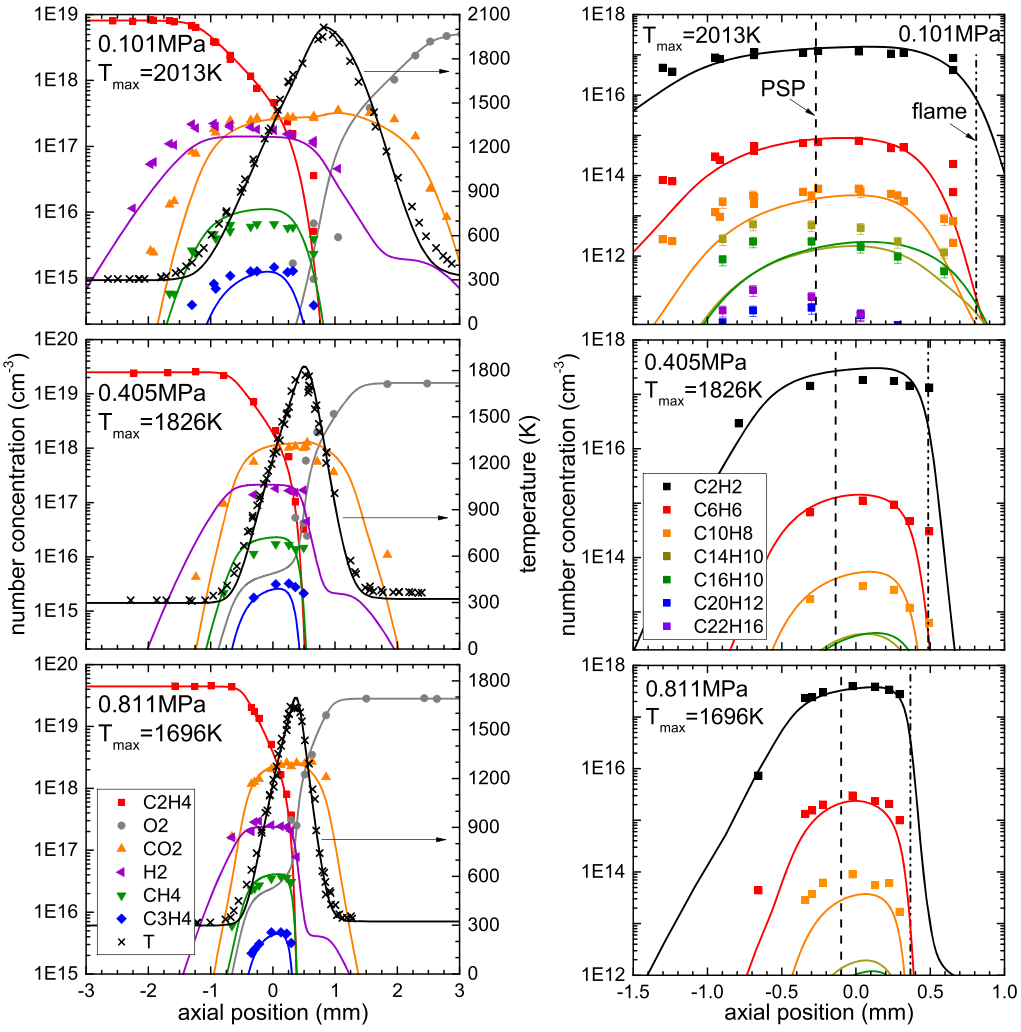


**Fig. 1.** (Left) Measured (symbols) and predicted (lines) spatial profiles of temperature and selected species relevant for modeling the Rayleigh scattering cross-section of the gas phase. (Right) Spatial profiles of selected species relevant to soot formation. Five-ring ($C_{20}H_{12}$) and six-ring ($C_{22}H_{16}$) PAHs that are quantified in the 0.101 MPa flame are not included in the model. The experimental data were presented originally in [15,27]. The right (left) vertical line in the right column panels marks the position of the flame (PSP).

## 3. Results

### 3.1. Beam steering corrections

One challenge of optical diagnostics in counterflow flames especially in high-pressure environments is the intrinsically steep temperature and density gradient, with ensuing steering of the laser beam. This work introduces a hybrid experimental and modeling technique to correct for beam steering using highly-controlled flames that exhibit a self-similar flame structure. We demonstrated that counterflow diffusion flames at constant global strain rate and stoichiometric mixture fraction are self-similar with respect to the dimensionless profiles of temperature and gas species, isolating $T_{max}$ as a controlling parameter to investigate soot formation [16,17]. In this work, starting from an incipiently sooting flame, we perturb it to decrease $T_{max}$ progressively, while maintaining constant $Z_{st}$=0.183 and $a = 50s^{-1}$ and stabilizing a non-sooting flame. So long as the temperature and the molar composition along the flame axis are provided by a partially validated model, the Rayleigh scattering contribution of the gas phase $Q_{\nu\nu}^{model}$ can be well predicted and, in the absence of beam steering, should agree well with the experimentally measured Rayleigh scattering signal $Q_{\nu\nu}^{meas}$of the non-sooting flame. If there is a discrepancy between $Q_{\nu\nu}^{meas}$ and $Q_{\nu\nu}^{model}$, one concludes that beam steering affected the calibration constant $C_{\nu\nu}^{cali}/S_{cali}$ in Eq. (1) by the ratio $Q_{\nu\nu}^{model}/Q_{\nu\nu}^{meas}$. The beam steering-corrected scattering coefficient along the burner axis is therefore evaluated as

$$Q_{\nu\nu}^{meas}|_{corr} = S_{meas}\frac{NC_{\nu\nu}^{cali}}{S_{cali}}\left[\frac{Q_{\nu\nu}^{model}}{Q_{\nu\nu}^{meas}}\right]_{non-sooting} \quad (5)$$

where the bracketed ratio is the beam steering correction factor. The correction of Eq. (5) results in a position-dependent calibration of the scattering intensity measured by the camera that relies on the local soot-free flame products as a calibration gas mixture that is already affected by beam steering. The correction factor is pressure-dependent but it applies to both sooting and non-sooting flames provided the flames maintain a self-similar structure and the departures from $T_{max}$ are modest. To determine $Q_{\nu\nu}^{model}$ we need profiles of temperature, reactants, and dominant species.

Figure 1 shows the 0.101 MPa, 0.405 MPa, and 0.811 MPa experimental profiles of these variables. The boundary conditions for these flames are listed in bold in Table 1 and the experimental data were presented originally in [15,27]. Lines represent model predictions of the CRECK kinetic model. In Fig. 1, the fuel stream approaches the flame from the left and oxidizer from the right with the zero axial position marking the gas stagnation plane (GSP)

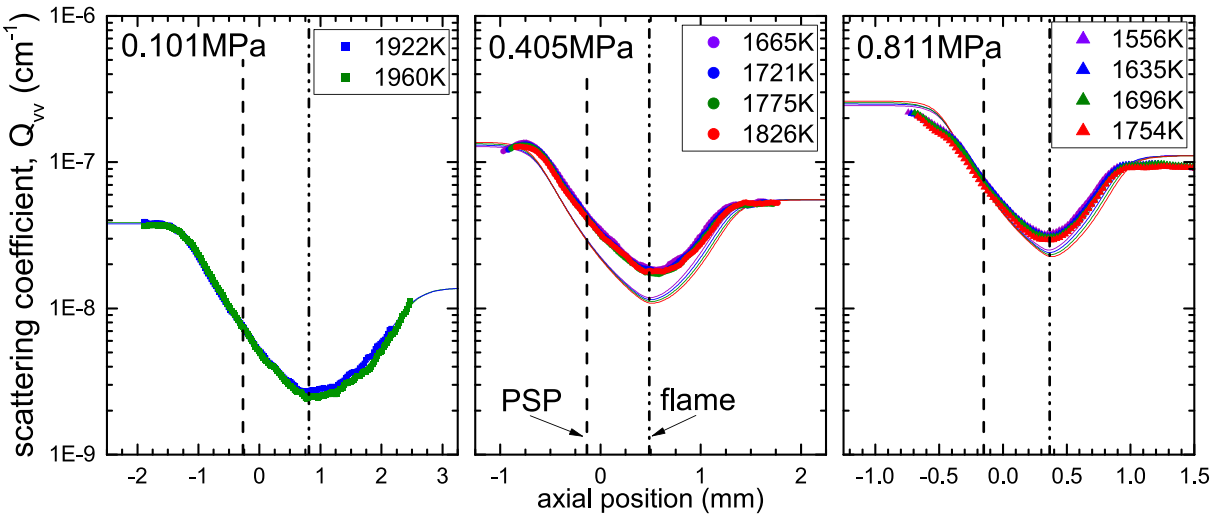


**Fig. 2.** Measured (symbols) and modeled (lines) profile of the scattering coefficient in self-similar flames where the contribution to the light scattering of soot particles is negligible or absent (i.e., non-sooting flames). The right (left) vertical line marks the position of the flame (PSP).

which is defined as the location where the axial velocity as determed from the model, is zero. At all pressures, the model predictions are in excellent agreement with the experimental data. To validate the model further in the context of soot formation, Figure 1 also shows the experimental profiles of acetylene, benzene ($C_6H_6$), and naphthalene ($C_{10}H_8$) for the same flames. The experimental profiles at 0.101 MPa also include phenanthrene ($C_{14}H_{10}$), pyrene ($C_{16}H_{10}$), benzopyrene ($C_{20}H_{12}$), and benzo[*ghi*]perylene ($C_{22}H_{12}$) [15]. Vertical lines mark the position of the flame (right) and Particle Stagnation Plane (PSP) (left). The PSP is defined as the location where the sum of the axial velocity and the thermophoretic velocity is zero; the latter is defined as $V_{th} = -0.538\nu\nabla\ln(T)$ and is calculated using the viscosity ($\nu$) provided by the model and the computed temperature profile. The model and experiments are in good agreement also for these species, except for phenanthrene that is underrepresented by a factor of three by the model. The CRECK kinetic model does not include species larger than pyrene ($C_{16}H_{10}$). The results in Fig. 1 serve as a partial validation of the one-dimensional model up to at least $C_{10}H_8$, which will be exploited when we compare the formation rate of soot to the production rate of key aromatics to identify feasible PAH precursors to soot inception. Furthermore, in computing $Q_{vv}^{model}$ we implicitly assume that the model is only marginally affected by the small changes in the composition of the fuel and oxidizer streams and by a less than 250 K change in $T_{max}$. As a result, we rely on the kinetic model with reasonable confidence to provide the flame temperature and molar concentration also for flames that were not sampled and analyzed with the GC/MS.

Figure 2 shows the measured (symbols) and predicted (lines) scattering coefficient of *non-sooting* flames at 0.101 MPa, 0.405 MPa, and 0.811 MPa for various $T_{max}$. Experimental data at each axial position is the average of 10 pixels (~225 µm) along the burner axis. The boundary conditions for these flames are italicized in Table 1. The soot forming zone would be bound between the vertical lines marking the position of the flame front and PSP, but soot formation is suppressed because of the low $T_{max}$ of these flames. If one neglects differences in the molar composition of the flames, one can scale $Q_{vv}^{model} \propto N \propto P/T$. Therefore, it is expected that $Q_{vv}^{model}$ systematically increases with increasing pressure and reaches a minimum at the flame front where the temperature is maximum. With a ~150 K (<10%) change in $T_{max}$ and a ~13% change in fuel mole fraction in the high-pressure flames, $Q_{vv}^{model}$ is nearly constant at each pressure because the flames maintain a self-similar structure and the molar composition is not significantly affected. We can expect that an additional modest increase in $T_{max}$ to promote soot formation will result in nearly identical scattering coefficient as these non-sooting flames in regions devoid of soot.

For light scattering measurements in the non-sooting flames at atmospheric pressure, where beam steering is absent/minimal, the measured Rayleigh scattering signal $Q_{vv}^{meas}$ reproduces $Q_{vv}^{model}$. At higher pressure, however, there is a consistent offset between $Q_{vv}^{meas}$ and $Q_{vv}^{model}$. It is important to note the qualitative agreement between experiments and model – the change of $T_{max}$ at constant pressure has a nearly inconsequential change on the scattering signal. The minimal uncertainty in the model predictions cannot explain this discrepancy in the high-pressure flames. Additionally, any temperature dependence of the scattering cross-section of species is estimated to cause less than a 5% variance at 532 nm [34]. Therefore, the discrepancy between $Q_{vv}^{meas}$ and $Q_{vv}^{model}$, which is present only in high-pressure flames, must be attributed to beam steering.

Figure 3 (top) shows the imaged Rayleigh signal of a non-sooting flame at each pressure to illustrate clearly the severity of beam steering as pressure increases. To orient the reader, we identify several features of each image: the dashed yellow line marks the position of the burner axis where measurements are performed; the dark region represents the high-temperature zone (i.e., the flame) which curves upward at the periphery because of buoyancy; the higher scattering signal below the flame is in the fuel stream resulting from the higher scattering cross-section of fuel molecules compared to the oxygen/nitrogen mixture from the top nozzle; the green arrow indicates the direction of propagation of the laser; the laser sheet enters the pressure chamber from the right with a uniform intensity profile. At 0.101 MPa (top image) beam steering is negligible and the laser profile exiting the pressure chamber (left) remains uniform. Above atmospheric pressure, the flame deflects the laser beam and the intensity profile is no longer uniform after passing through the flame, which is particularly visible at 0.811 MPa with the appearance of distinct stripes to the left of the burner axis.

The graph at the bottom of Fig. 3 shows the experimentally determined correction factor $Q_{vv}^{model}/\ Q_{vv}^{meas}$ for non-sooting flames at the three pressures obtained from the data in Fig. 2. As expected, the ratio is near unity throughout the flames at atmospheric pres-

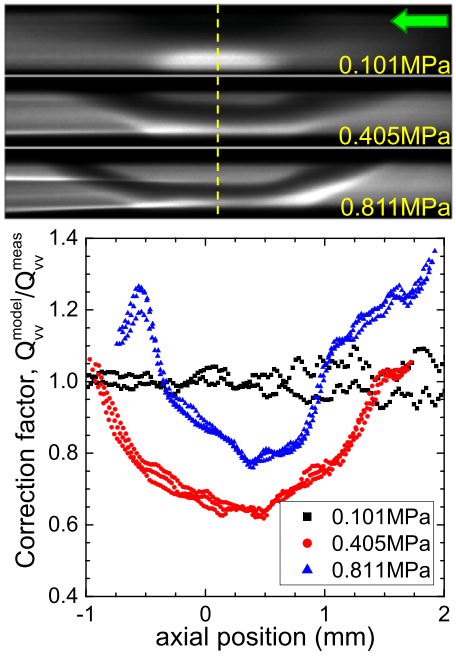


**Fig. 3.** Top: Rayleigh signal of a non-sooting flame at each pressure. The laser path is from right to left as indicated by the green arrow and the yellow dashed line marks the burner axis. Bottom: spatially-dependent beam steering correction factor at three different pressures to account for the increasingly more severe effect of beam steering as visible in the images above. (For interpretation of the references to colour in this figure legend, the reader is referred to the web version of this article.)

sure, implying that the gas phase Rayleigh scattering contribution is well predicted and beam steering is negligible; the larger variability in the high-temperature region ($0.5<z<2.0$) is due to the small scattering coefficient and the subsequent low signal-to-noise ratio. Above atmospheric pressure, the ratio $Q_{vv}^{model}/\ Q_{vv}^{meas}$ is non-unity but does not vary by more than 3% at a given position for flames with different $T_{max}$ but constant pressure. Fig. 3 reveals that a single spatially- and pressure-dependent correction factor of the measured scattering signal can be applied to the results obtained for flames perturbed in the chosen range of $T_{max}$. These data provide the beam steering correction factor on incipiently sooting flames, that is, on flames that were perturbed progressively to *increase* $T_{max}$ while maintaining constant $Z_{st}$=0.183 and $a=50\text{s}^{-1}$.

### 3.2. Results in sooting flames

Profiles of the corrected scattering coefficient measured in all sooting flames are shown in Fig. 4. The measured scattering coefficient ($Q_{vv}^{meas}$, symbols) is in good agreement with the one predicted for the gas-phase contribution ($Q_{vv}^{model}$, lines) in regions devoid of soot, confirming our previous expectation that a modest increase in $T_{max}$ and the consequent presence of soot particles does not affect significantly the scattering coefficient in regions devoid of soot. Only one line is shown at each pressure in Fig. 4 because changes in $Q_{vv}^{model}$ for a less than 250 K change in maximum flame temperature are nearly indistinguishable (see Fig. 2). In the soot forming region, bound between the flame and PSP, $Q_{vv}^{meas}$ begins to depart from $Q_{vv}^{model}$ and the departure is progressively more drastic with increasing $T_{max}$. $Q_{vv}^{meas}$ reaches a maximum at the PSP, rapidly decreasing to $Q_{vv}^{model}$ on the fuel side (left) of the PSP where no soot is present. Experimental data are truncated when the scattered signal is within 10% of the camera background noise. The limited (12-bit) dynamic range of the camera makes it impossible to quantify the scattering coefficient over the full-scale range which can

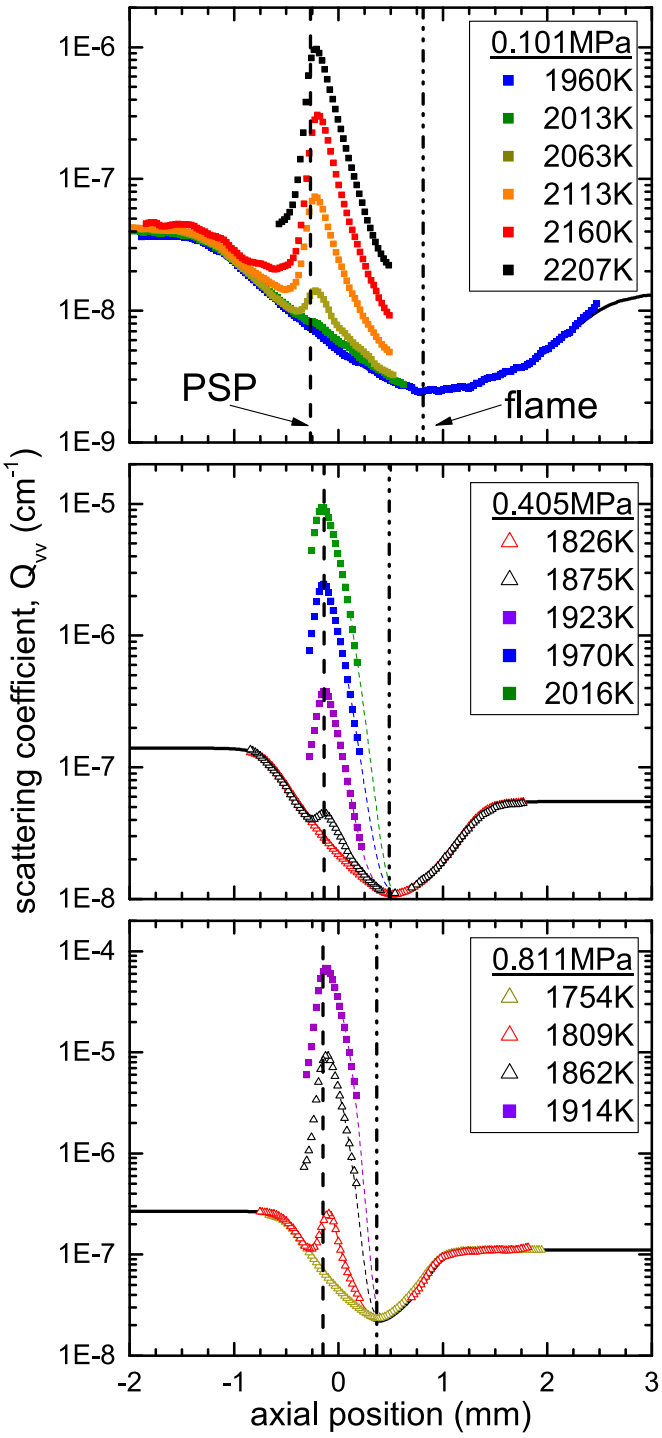


**Fig. 4.** Scattering coefficient for all flames investigated after correcting for beam steering. Dotted colored lines represent data that have been extrapolated to a location near the flame front where the contribution from soot is expected to be negligible. The right (left) vertical line marks the position of the flame (PSP).

span three orders of magnitude or more for the flames at the highest temperatures. As a result, the experimental profiles for flames at sufficiently high temperatures show no data overlapping with the gas phase boundary conditions. To recover partially the high-pressure data in the high-temperature region, the dotted *lines* in Fig. 4 represents an extrapolation of $Q_{vv}^{meas}$. Clearly, we expect $Q_{vv}^{meas}$ to approach the gas phase value close to the flame front where the soot contribution must have vanished. The experimental $Q_{vv}^{soot}$

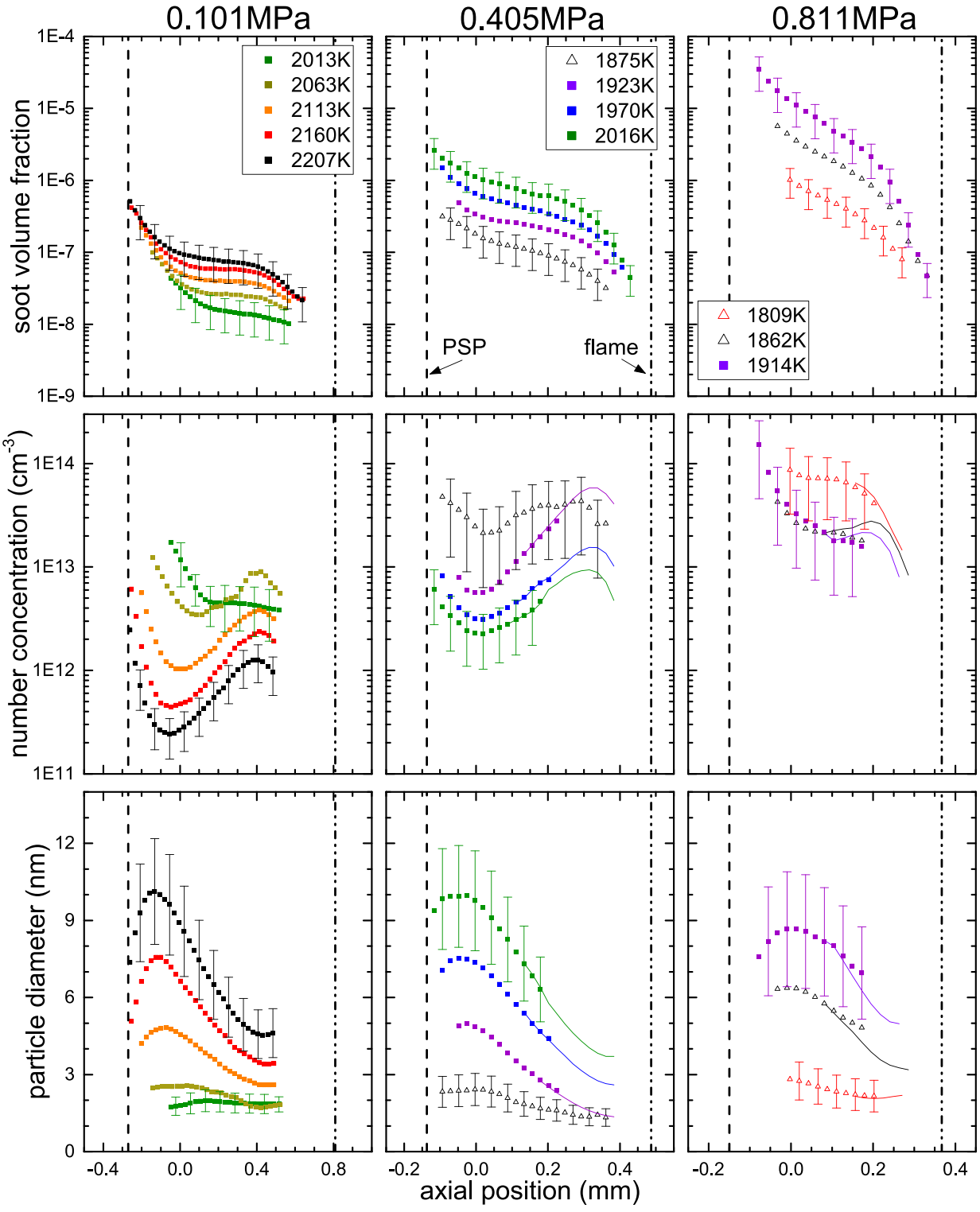


**Fig. 5.** Measured soot volume fraction (top) from [16], number concentration (middle) and particle size (bottom) under the assumption of monodisperse size distribution, at pressures of 0.101 MPa (left), 0.405 MPa (middle), and 0.811 MPa (right). Solid lines rely on the extrapolated soot scattering coefficient in Fig. 4. The right (left) vertical line marks the position of the flame (PSP).

is fitted with a Gaussian curve and restricted to be less than 1% of the gas phase at the flame front. A Gaussian curve fitting the rightmost set of experimental data close to the flame provided the best shape-preserving fit for extrapolation to the flame front. This approach allows us to extend our analysis into the high-temperature region, where the experimental signal has fallen to the noise limit. Since the extrapolated data are subject to larger uncertainties, we will alert the reader when the discussion relies on such data.

Figure 5 summarizes the soot measurements in all counterflow diffusion flames. Soot volume fraction measurements were acquired by pyrometry as reported in [16,17]. Symbols represent experimental data and solid lines represent data that rely on the

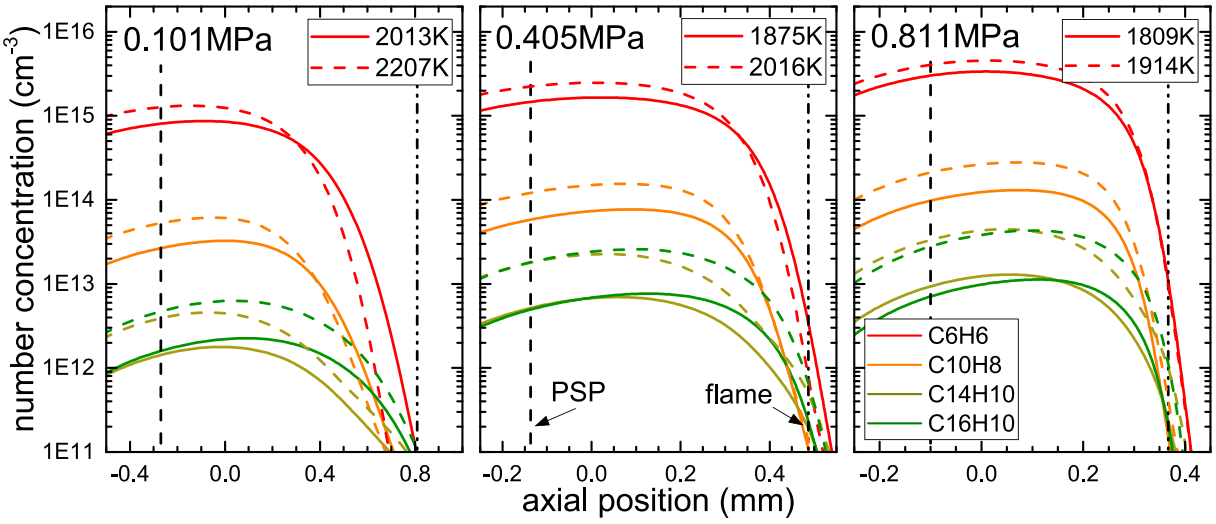


**Fig. 6.** Number concentrations of aromatic species at different pressures. At each pressure, results are shown for two flames, the one at the lowest peak temperature at which soot is quantified (solid line) and the other at the highest considered peak temperature (dashed lines). The right (left) vertical line marks the position of the flame (PSP) (The reader is referred to the web version of this article for a colored version of this figure in which the identification of each curve is clear cut.)

extrapolated $Q_{vv}^{soot}$. To avoid excessive clutter, error bars representing 95% confidence intervals are provided only for the lowest and highest $T_{max}$ and we do not consider potential errors associated with the uncertainty of extrapolation. Data for the lowest $T_{max}$-flames in Fig. 4 (1960 K at 0.101 MPa, 1826 K at 0.405 MPa, and 1754 K at 0.811 MPa) are not shown because the difference between $Q_{vv}^{meas}$ and $Q_{vv}^{model}$ is within the noise limit. The reported number concentration and particle diameter are calculated under the assumption of monodisperse particles. Several observations are in order:

i) as expected, soot nucleates near the flame front on the right, experiencing continuous growth in its (right to left) path towards the PSP until it is convected away radially, with essentially no opportunity to oxidize;
ii) as pressure increases, there is a significant increase in soot volume fraction and number concentration;
iii) the particle size is smallest, at a few nanometers, close to the flame front where soot inception begins and remains below 9–11 nm in all flames after soot particles have enough time to grow; and
iv) at the lowest $T_{max}$, regardless of pressure, the particle size is nearly constant which is reminiscent of the "nucleating flame" reported in [6], where surface growth and coagulation are almost entirely suppressed and soot mass (volume fraction) increases only by particle nucleation.

At atmospheric pressure, the number concentration has a local maximum near the flame front. As the residence time increases, moving from the flame front towards the PSP, the number concentration decreases, and particle size increases because of ongoing coagulation. In proximity to the PSP, the trends are reversed: number concentration rapidly increases and particle diameter decreases. These trends are consistent with the "low-temperature" soot forming mechanism that was rationalized in [16,17] from just volume fraction and dispersion exponent measurements. Initially, coagulation enlarges the particle diameter and decreases the particle number concentration, whereas surface growth reactions increase both the volume fraction and particle diameter. The low-temperature soot forming mechanism which activates at temperatures below 1600 K [17] becomes the dominant mechanism near the PSP and it results in an increase in number concentration and a decrease in particle diameter. This low-temperature mechanism is due to *nucleation* rather than *growth* involving PAHs that was speculated to be the mechanism at high pressures [16,41]. Diagnostic limitations prevent the quantification of soot number concentration close to the flame front in the high-temperature 0.405 MPa flames, but the extrapolation on $Q_{vv}^{soot}$ suggest that the profiles of the number concentration of soot particle are qualitatively similar to the ones measured at 0.101 MPa. At 0.811 MPa, the measured number concentration profiles monotonically increase and the particle diameter shows a mild increase relative to the 0.101 MPa and 0.405 MPa trends. The 0.811 MPa data suggests that the low-temperature nucleation mechanism is more active at higher pressure and is nearly balanced by particle coagulation before the low-temperature nucleation takes over in proximity to the PSP.

As to the temperature effect at a fixed pressure, it invariably results in an increase in soot volume fraction and particle sizes and a decrease in number concentration. Particle sizes remain within the 2–11 nm range and the number concentration of incipient soot particles in proximity to the flame front is approximately invariant with pressure.

### 3.3. Soot nucleation rate versus PAH dimerization rate

The goal of this section is to assess the soot nucleation rate in each flame and compare it to the dimerization rate of critical aromatics to identify feasible soot precursors. To that end, we first illustrate the effect of temperature and pressure on PAHs in Fig. 6, showing the computed number concentration of aromatic species for flames at the highest and lowest $T_{max}$ for which soot is quantified. Note that the larger PAHs are more sensitive to changes in $T_{max}$ and such a sensitivity increases with pressure. Specifically, benzene increases by approximately 30% whereas pyrene increases by a factor of three, when $T_{max}$ increases by ~200 K at 0.101 MPa and by ~100 K at 0.811 MPa. This trend is consistent with the increased sensitivity of soot volume fraction at higher pressure (Fig. 5). At constant $T_{max}$, a four-fold increase in pressure (i.e., comparing the 0.101MPa-2013 K flame and the 0.405MPa-2016 K flame) results in a two-fold increase in benzene concentration but a factor of four increase in pyrene concentration and approximately a factor of fifty increase in soot concentration.

A comparison of Figs. 5 and 6 demonstrates that there is a disparity in the molar abundance of soot and large PAHs, such as pyrene or larger ones [9,10,12], that are often postulated as

the precursors to soot, with the soot being at much larger number concentrations. This disparity makes it difficult to justify that these large species are those driving the nucleation of soot. Rather, we argue that small aromatic species such as one-ring or two-ring compounds are controlling the soot nucleation rate from non-aromatic fuels, as further illustrated in the ensuing discussion.

Using the partially validated profiles of concentration of PAHs, now we can calculate the profiles of their dimerization rate based on the gas kinetic (self-)collision rate according to

$$\dot{\omega}_{DIM} = \eta \sqrt{\frac{4\pi k_B T}{M_{PAH}}} \sigma^2 \Omega^*(T^*) N_a^2 [PAH]^2, \tag{6}$$

where $\eta$, $k_B$, $N_a$, $M_{PAH}$, $\sigma$,$\Omega^*(T^*)$ are the dimerization efficiency (i.e., the fraction of collisions that result in dimerization events), Boltzmann constant, the Avogadro number, the mass, the collision diameter, and the reduced collision integral [42] of the PAH in question. [PAH] is the molar concentration of species 'PAH' and $\dot{\omega}_{DIM}$ has units of number concentration ($cm^{-3}$). The dimerization efficiency is assumed $\eta$ =1% for all considered PAHs, which is likely an overestimate, particularly for the smallest ones (e.g., benzene and naphthalene), which are expected to have much lower dimerization efficiency [11,43,44].

Turning our attention to the soot nucleation rate, $\frac{\partial N_S}{\partial t}|_{nucl}$, we can recover it from the governing equation for the number concentration $N_S$ of soot particles along the axis, $z$, of the axis-symmetric flow field, namely,

$$\frac{\partial N_S}{\partial t}|_{nucl} - \gamma_{coag} \frac{1}{2} K_{coll} N_s^2 = \frac{d}{dz}[N_s \cdot (V_z + V_{th} + V_P)] + N_s \cdot \frac{d\ V_r}{dr}. \tag{7}$$

The second term on the LHS is the destruction rate due to the coagulation of particles that are monodisperse in size. $\gamma_{coag}$ is the collision efficiency (the probability that particles stick together once they collide). The collision kernel, $K_{coll}$, is calculated using the expression

$$K_{coll} = 8\pi d \cdot\ D_P \left\{ \frac{d}{d + \sqrt{2} \cdot g} + \frac{8\ D_P}{\sqrt{2} c \cdot d} \right\},$$

with

$$g\ = \frac{\pi c}{24 d \cdot D_P} \left\{ \left( d + \frac{8 D_P}{\pi c} \right)^3 - \left[ d^2 + \left( \frac{8 D_P}{\pi c} \right)^2 \right]^{3/2} \right\} - d, \tag{8}$$

and

$$c = \sqrt{\frac{48 k_B T}{\pi^2 \rho_s d^3}},$$

and $d$ is the measured particle size. The thermophoretic velocity is estimated by $V_{th} = -0.538 \cdot \nu \cdot\ d\ln(T)/dz$ and the particle Brownian velocity by $V_P = -D_P \cdot\ d\ln(N_s)/dz$. The value of the Brownian diffusivity is calculated as a function of the measured particle diameter by

$$D_P = \left( \frac{k_B T}{3\pi \rho_s \nu d} \right) \left[ 1 + 2Kn \left( A + B\ e^{-\frac{C}{Kn}} \right) \right]. \tag{9}$$

The Knudsen number, $Kn$, is the ratio of gas mean free path to particle diameter, and A, B, and C are empirical constants set equal to 1.257, 0.4, and 0.55, respectively [45]. The density of soot is assumed constant at $\rho_s$=1.5 g/cm$^3$. The temperature $T$, axial velocity $V_z$, radial gradient of the radial velocity $dV_r/dr$, and viscosity $\nu$ in Eqs. (7)-(9) are extracted from the one-dimensional model.

The evaluation of Eqs. (6)–(7) in various flames is presented in Fig. 7. The grey shaded region and the dashed one pertain to the use of the experimental data and extrapolated data of $Q_{vv}^{soot}$, respectively. They are obtained from Eq. (7) by assuming $\gamma_{coag}$= 2% (lower bound) and 100% (upper bound). The data in Fig. 7 are useful to identify trends on the effect of pressure on the number nucleation rate of soot and its precursors. We shall focus on the (blue) shaded region next to the flame corresponding to the hot soot nucleation zone. In the inception zone, and throughout most of the soot forming region in the low $T_{max}$ high-pressure flames, it is clear that dimers consisting of only one or two rings have formation rates comparable to soot whereas the low abundance of the larger aromatics cannot account for it. While the inception zone in the 0.405 MPa and 0.811 MPa pressure flames relies on extrapolation for the intermediate and high peak temperature, the experimental data alone are sufficient to conclude that the nucleation rate of soot is consistently at the level of the dimerization rate of two-ring aromatics, especially in the most lightly incipient sooting conditions at low $T_{max}$. Therefore, our principal observation does not depend significantly on the extrapolation that was discussed in connection with Fig. 4 and it holds regardless of pressure and temperature. As already mentioned, we also emphasize that the assumption of 1% dimerization efficiency is generous for PAHs smaller than pyrene [43]. But, even with the low estimate of the soot nucleation rate deriving from the assumption of size monodispersity and a high estimate of the molecular dimerization rate, there remains a large disparity between the two when considering PAHs larger than three-rings. A four-fold increase in pressure from 0.101 MPa increases the soot number nucleation rate and PAH dimerization rate in flames with constant peak temperature, which is primarily a concentration effect on the bimolecular collision rates. A similar but perhaps less pronounced effect is observed in the higher (0.405–0.811 MPa) pressure range (see, for example, data for $T_{max}$=1875 K at $P$=0.405 MPa, and those for $T_{max}$=1862 K at $P$=0.811 MPa; see also data for $T_{max}$=2013 K at $P$=0.101 MPa, and those for $T_{max}$=2016 K at $P$=0.405 MPa). Changes in pressure and temperature tend to be more consequential on large aromatics.

The same considerations apply to the number nucleation rate associated with the low-temperature nucleation mechanism that is active between the GSP at the origin of the abscissa and the PSP where the left vertical line is located. This is particular true for the low temperature flames in the top row of Fig. 7, the so-called nucleation flames, in which particle size is approximately constant and size distribution effects are anticipated to be modest: for such flames the above discussion holds throughout the soot laden region. On the other hand, in the graphs of some of the other flames, such as those at the highest temperature at 0.101 MPa and 0.405 MPa in the bottom row of Fig. 7, the number nucleation rate of the low-temperature mechanism appears to be at the level of the dimerization rate of 3–4 ringed aromatics. However, the assumption of monodisperse particle sizes used in the data analysis is likely to be inaccurate in these cases, since the nucleating particles are detected alongside larger particles that underwent coagulation and were transported from the high-temperature region, at positive values of the abscissa. In consideration of the fact that the PAH dimerization efficiency is largely overestimated, one can safely speculate that the low-temperature number nucleation rate is also controlled by aromatics composed of one or two rings even in these cases.

It is important to consider not only the formation rates from individual species but the cumulative combination of isomers of similar size. From the GC measurements in the 0.101MPa-2013 K flame [15] (top left panel of Fig. 7), it was concluded that the cumulative number concentration of *all* species composed of at least three aromatic rings is a factor of two or three below the one of naphthalene ($C_{10}H_8$). Additionally, radical species are predicted to exist at concentrations of at least one order of magnitude lower than their respective stable counterparts. Therefore, it is estimated

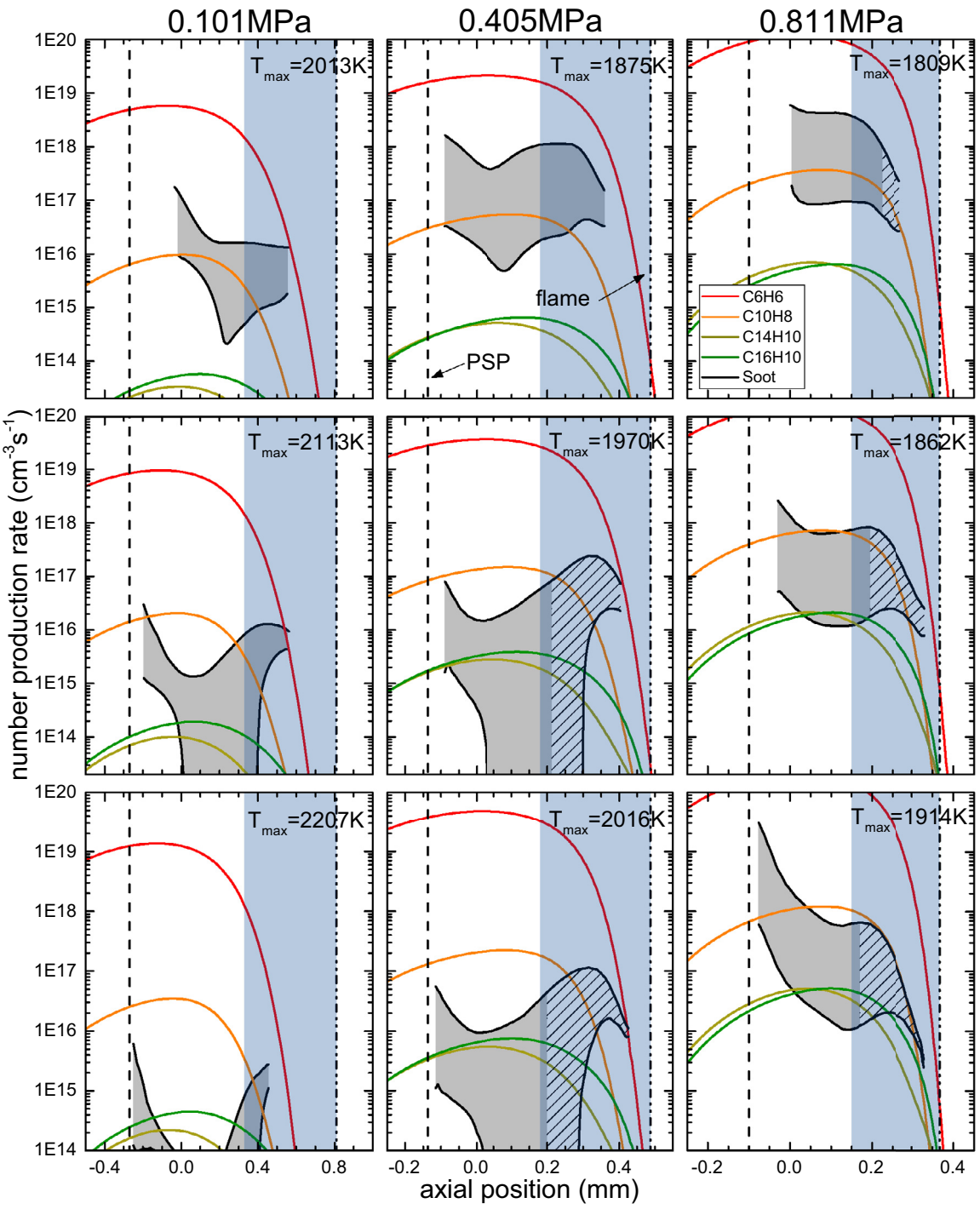


**Fig. 7.** Number production rate of soot compared to the dimerization rate of various PAHs calculated by assuming 1% dimerization efficiency. The grey shaded region (and the dashed one) represent soot production rate for a monodisperse size distribution by assuming $\gamma_{coag}$= 2% (lower bound) and 100% (upper bound). They pertain to the use of the experimental data (grey region) and extrapolated data of $Q_{vv}^{soot}$ (dashed region). The right (left) vertical line marks the position of the flame (PSP). (For interpretation of the references to colour in this figure legend, the reader is referred to the web version of this article.)

by the model that the dimerization/clustering of all isomers with more than 13 carbon atoms would result in nucleation rates of soot below the ones predicted for the dimerization of naphthalene. It appears that only the smallest aromatics are present at sufficient concentrations to account for the measured soot nucleation rate. In fact, soot nucleation via dimerization can be narrowed down perhaps to only single-ring aromatic compounds if one considers smaller, more realistic, dimerization efficiencies for the smallest PAHs [43]. Even the near-irreversible collision between a PAH molecule and a PAH radical [8] must involve small aromatic compounds because of the low concentration of radicals predicted by the kinetic model. The results in Fig. 7 suggest that, although large PAHs are expected to contribute to the overall growth of the incipient soot particles, the role of the smaller PAHs and their modeling is more important to predict soot nucleation rates in flames fueled by aliphatic fuels.

A seemingly peculiar trend is exhibited in the coagulation region of the 0.101 MPa and 0.405 MPa high-$T_{max}$ flames because the nucleation rate of soot drops drastically in the logarithmic scale of the graph ordinate. This is a consequence of vanishingly small values of the *number nucleation rate* (of course, the nucleation rate cannot but remain positive in both terms of mass and number throughout the soot forming region) compared to the destruction rate due to the coagulation. The latter is the most intense in these flame conditions compared to the others and only estimated in our data analysis.

In conclusion, the comparison of the number nucleation rates of soot and dimerization rates of aromatic compounds in high-pressure flames confirms results that were reported in [15] at atmospheric pressure: the rate-limiting step in the sequence that ultimately controls the nucleation rate appears to be the formation of either single-ring aromatic compounds or, at most, two-ring aromatic compounds. Certainly larger PAHs play a role in the overall formation of soot, but not in the very early stage of soot nucleation, in contrast with the long-standing hypothesis that chemical bond-building and clustering of relatively *large* aromatic systems such as pyrene trigger incipient soot [8–12]. Large PAHs are likely to be short-lived intermediates that participate in the overall growth of the incipient soot particles by adsorbing quickly on the initial dimers, leading to much larger peri-condensed PAHs with the necessary resonance stabilization that prevents their fragmentation [4], consistently with the presence of PAHs of several hundred Da in the ordered stacks and disordered clusters that constitute soot nanoparticles [43,46].

## 4. Conclusions

Light scattering measurements in counterflow ethylene diffusion flames in the 0.101–0.811 MPa pressure range, in conjunction with previously reported measurements of soot volume fraction and predictions of the spatial sequencing of species from the parent molecule to multi-ring PAHs using a partially validated chemistry model, yielded an assessment of the PAHs controlling soot nucleation rate. Flames were studied at constant stoichiometric mixture fraction, $Z_{st}$=0.183, and global strain rate $a$=50s$^{-1}$ to isolate pressure and peak flame temperature as key controlling parameters. Principal conclusions follow.

- Non-sooting flames can be used to determine a pressure-dependent beam steering correction factor. Provided that both sooting and non-sooting flames maintain a self-similar flame structure, these corrections can be applied to sooting flames, to improve the accuracy of measuring the gas phase Rayleigh scattering contribution and ultimately allow for the quantification of the soot particles in the 2–3 nm range in challenging pressurized counterflow flame conditions.
- A comparison of the soot number nucleation rate and dimerization rate of PAHs reveals that the soot nucleation rate is consistent only with the dimerization of one- and two-ring PAHs and that large PAHs (composed of three or more aromatic rings) are not key intermediates to soot inception in ethylene fueled flames.
- A four-fold increase in pressure from 0.101 MPa to 0.405 MPa increases soot nucleation rate and PAH dimerization rate in flames with constant peak temperature, which is primarily a concentration effect on bimolecular collision rates; a similar but less pronounced effect is observed in the higher (0.405–0.811 MPa) pressure range. Changes in pressure and temperature tend to be progressively more consequential on aromatics of increasing molecular weight and soot.
- Soot particle sizes remain relatively small ($d$<11 nm) despite the fact that the volume fraction spans over three orders of magnitude in all investigated flames. An increase in $T_{max}$ at constant pressure increases volume fraction and particle sizes and decreases soot number concentration. Particle sizes (number concentration) decrease (increase) in proximity of the particle stagnation plane where a low-temperature soot forming mechanism is activated.
- The number nucleation rate of the low-temperature mechanism is also consistent only with the dimerization of one- and two-ring PAHs and faster than that of larger aromatics.

## Declaration of Competing Interest

The authors declare that they have no known competing financial interests or personal relationships that could have appeared to influence the work reported in this paper.

## Acknowledgments

K.G. and A.G. acknowledge the support of the National Science Foundation (CBET-1853150) and Yale University. Authors declare no competing interests.

## References

[1] Y. Wang, S.H. Chung, Soot formation in laminar counterflow flames, Prog. Energy Combust. Sci. 74 (2019) 152–238.
[2] H. Richter, J.B. Howard, Formation of polycyclic aromatic hydrocarbons and their growth to soot - a review of chemical reaction pathways, Prog. Energy Combust. Sci. 26 (4–6) (2000) 565–608.
[3] A.E. Karatas, O.L. Gulder, Soot formation in high pressure laminar diffusion flames, Prog. Energy Combust. Sci. 38 (6) (2012) 818–845.
[4] K.O. Johansson, M.P. Head-Gordon, P.E. Schrader, K.R. Wilson, H.A. Michelsen, Resonance-stabilized hydrocarbon-radical chain reactions may explain soot inception and growth, Science 361 (6406) (2018) 997–1000.
[5] B. Zhao, Z. Yang, Z. Li, M.V. Johnston, H. Wang, Particle size distribution function of incipient soot in laminar premixed ethylene flames: effect of flame temperature, Proc. Combust. Inst. 30 (1) (2005) 1441–1448.
[6] P. Desgroux, A. Faccinetto, X. Mercier, T. Mouton, D. Aubagnac Karkar, A. El Bakali, Comparative study of the soot formation process in a "nucleation" and a "sooting" low pressure premixed methane flame, Combust. Flame 184 (2017) 153–166.
[7] K.O. Johansson, J.Y.W. Lai, S.A. Skeen, D.M. Popolan-Vaida, K.R. Wilson, N. Hansen, A. Violi, H.A. Michelsen, Soot precursor formation and limitations of the stabilomer grid, Proc. Combust. Inst. 35 (2) (2015) 1819–1826.
[8] M. Frenklach, A.M. Mebel, On the mechanism of soot nucleation, Phys. Chem. Chem. Phys. 22 (2020) 5314–5331.
[9] M. Frenklach, H. Wang, Detailed modeling of soot particle nucleation and growth, Symp. (Int.) Combust. 23 (1) (1991) 1559–1566.
[10] M.R. Kholghy, N.A. Eaves, A. Veshkini, M.J. Thomson, The role of reactive PAH dimerization in reducing soot nucleation reversibility, Proc. Combust. Inst. 37 (1) (2019) 1003–1011.
[11] Y. Wang, A. Raj, S.H. Chung, Soot modeling of counterflow diffusion flames of ethylene-based binary mixture fuels, Combust. Flame 162 (3) (2015) 586–596.
[12] A. Faccinetto, C. Irimiea, P. Minutolo, M. Commodo, A. D'Anna, N. Nuns, Y. Carpentier, C. Pirim, P. Desgroux, C. Focsa, X. Mercier, Evidence on the formation of dimers of polycyclic aromatic hydrocarbons in a laminar diffusion flame, Commun. Chem. 3 (1) (2020) 1–8.
[13] A. D'Anna, A. Violi, A kinetic model for the formation of aromatic hydrocarbons in premixed laminar flames, Symp. (Int.) Combust. 27 (1) (1998) 425–433.
[14] H. Miller, K.C. Smyth, W.G. Mallard, J.H. Miller, K.C. Smyth, W.G. Mallard, Calculations of the dimerization of Aromatic Hydrocarbons: implications for soot formation, Symp. (Int.) Combust. 20 (1) (1984) 1139–1147.
[15] K. Gleason, F. Carbone, A.J. Sumner, B.D. Drollette, D.L. Plata, A. Gomez, Small aromatic hydrocarbons control the onset of soot nucleation, Combust. Flame 223 (2021) 398–406.
[16] K. Gleason, F. Carbone, A. Gomez, Pressure and temperature dependence of soot in highly controlled counterflow ethylene diffusion flames, Proc. Combust. Inst. 37 (2) (2019) 2057–2064.
[17] K. Gleason, F. Carbone, A. Gomez, Effect of temperature on soot inception in highly controlled counterflow ethylene diffusion flames, Combust. Flame 192 (2018) 283–294.
[18] L. Figura, A. Gomez, Laminar counterflow steady diffusion flames under high pressure (P<3MPa) conditions, Combust. Flame. 159 (1) (2012) 142–150.
[19] H.M.F. Amin, W.L. Roberts, Soot measurements by two angle scattering and extinction in an N2-diluted ethylene/air counterflow diffusion flame from 2 to 5atm, Proc. Combust. Inst. 36 (1) (2017) 861–869.
[20] B.G. Sarnacki, H.K. Chelliah, Sooting limits of non-premixed counterflow ethylene/oxygen/inert flames using LII: effects of flow strain rate and pressure (up to 30 atm), Combust. Flame 195 (2018) 267–281.

[21] X. Xue, P. Singh, C.J. Sung, Soot formation in counterflow non-premixed ethylene flames at elevated pressures, Combust. Flame 195 (2018) 253–266.
[22] S.A. Kaiser, J.H. Frank, M.B. Long, Use of Rayleigh imaging and ray tracing to correct for beam-steering effects in turbulent flames, Appl. Opt. 44 (31) (2005) 6557–6564.
[23] S.A. Steinmetz, T. Fang, W.L. Roberts, Soot particle size measurements in ethylene diffusion flames at elevated pressures, Combust. Flame 169 (2016) 85–93.
[24] W.L. Flower, C.T. Bowman, Soot production in axisymmetric laminar diffusion flames at pressures from one to ten atmospheres, Symp. (Int.) Combust. 21 (1) (1988) 1115–1124.
[25] K.A. Thomson, O.L. Gulder, E.J. Weckman, R.A. Fraser, G.J. Smallwood, D.R. Snelling, Soot concentration and temperature measurements in co-annular, nonpremixed $CH_4$/air laminar flames at pressures up to 4MPa, Combust. Flame 140 (3) (2005) 222–232.
[26] H.I. Joo, O.L. Gulder, Experimental study of soot and temperature field structure of laminar co-flow ethylene-air diffusion flames with nitrogen dilution at elevated pressures, Combust. Flame 158 (3) (2011) 416–422.
[27] F. Carbone, K. Gleason, A. Gomez, Pressure effects on incipiently sooting partially premixed counterflow flames of ethylene, Proc. Combust. Inst. 36 (1) (2017) 1395–1402.
[28] L. Figura, A. Gomez, Structure of incipiently sooting ethylene-nitrogen counterflow diffusion flames at high pressures, Combust. Flame. 161 (6) (2014) 1587–1603.
[29] ANSYS CHEMKIN-Pro Release 2019 R2.
[30] C. Saggese, S. Ferrario, J. Camacho, A. Cuoci, A. Frassoldati, E. Ranzi, H. Wang, T. Faravelli, Kinetic modeling of particle size distribution of soot in a premixed burner-stabilized stagnation ethylene flame, Combust. Flame 162 (9) (2015) 3356–3369.
[31] X. Han, S.K. Aggarwal, K. Brezinsky, Effect of unsaturated bond on NOx and PAH formation in n-heptane and 1-heptene triple flames, Energy Fuels 27 (1) (2013) 537–548.
[32] W.H. Dalzell, A.F. Sarofim, Optical constants of soot and their application to heat-flux calculations, J. Heat Transf. 91 (1) (1969) 100–104.
[33] C.J. Dasch, Continuous-wave probe laser investigation of laser vaporization of small soot particles in a flame, Appl. Opt. 23 (13) (1984) 2209.
[34] J.A. Sutton, J.F. Driscoll, Rayleigh scattering cross sections of combustion species at 266, 355, and 532nm for thermometry applications, Opt. Lett. 29 (22) (2004) 2620–2622.
[35] G. Sutton, A. Levick, G. Edwards, D. Greenhalgh, A combustion temperature and species standard for the calibration of laser diagnostic techniques, Combust. Flame 147 (1–2) (2006) 39–48.
[36] A. D'Alessio, Laser light scattering and fluorescence diagnostics of rich flames produced by gaseous and liquid fuels, in: D.C. Siegla (Ed.), Particulate Carbon, Springer, 1981, pp. 207–259.
[37] M.P. Bogaard, A.D. Buckingham, R.K. Pierens, A.H. White, Rayleigh scattering depolarization ratio and molecular polarizability anisotropy for gases, J. Chem. Soc. Faraday Trans. 1 Phys. Chem. Condens. Phases 74 (1978) 3008–3015.
[38] H.A. Michelsen, P.E. Schrader, F. Goulay, Wavelength and temperature dependences of the absorption and scattering cross sections of soot, Carbon N. Y. 48 (8) (2010) 2175–2191.
[39] P.A.M. Kalt, M.B. Long, Image Processing For Mac OS X, 2015 www.oma-x.org.
[40] B. Ma, M.B. Long, Absolute light calibration using S-type thermocouples, Proc. Combust. Inst. 34 (2) (2013) 3531–3539.
[41] N.A. Eaves, A. Veshkini, C. Riese, Q. Zhang, S.B. Dworkin, M.J. Thomson, A numerical study of high pressure, laminar, sooting, ethane-air coflow diffusion flames, Combust. Flame 159 (10) (2012) 3179–3190.
[42] P.D. Neufeld, A.R. Janzen, R.A. Aziz, Empirical equations to calculate 16 of the transport collision integrals $\Omega(l,s)^*$ for the Lennard-Jones (12–6) potential, J. Chem. Phys. 57 (3) (1972) 1100–1102.
[43] A. Raj, M. Sander, V. Janardhanan, M. Kraft, A study on the coagulation of polycyclic aromatic hydrocarbon clusters to determine their collision efficiency, Combust. Flame 157 (3) (2010) 523–534.
[44] W. Pejpichestakul, A. Frassoldati, A. Parente, T. Faravelli, Kinetic modeling of soot formation in premixed burner-stabilized stagnation ethylene flames at heavily sooting condition, Fuel 234 (2018) 199–206.
[45] S.K. Friedlander, Smoke, Dust and Haze: Fundamentals of Aerosol Behavior, John Wiley & Sons Inc, 1977.
[46] R.S. Jacobson, A.R. Korte, A. Vertes, J.H. Miller, The molecular composition of soot, Angew. Chem. Int. Ed. 132 (11) (2020) 4514–4520.